Facile Synthesis Mn2O3 Nanorod Arrays: A Significant Material for Supercapacitor Electrode Application

S Nelson Amirtharaj (snelsamir@gmail.com)

Department of Chemistry, T. B. M. L. College, Porayar, Tamilnadu, India-609307 https://orcid.org/0000-0001-8284-4423

M. Mariappan

Department of Chemistry, Thiru. Vi. Ka. Govt. Arts College, Thiruvarur, Tamilnadu, India-610003

Research Article

Keywords: Mn2O3 nanorod arrays, energy storage, Supercapacitor, sonochemical

Posted Date: February 15th, 2021

DOI: https://doi.org/10.21203/rs.3.rs-220726/v1

Facile Synthesis Mn_2O_3 Nanorod Arrays: A Significant Material for Supercapacitor Electrode Application

S. Nelson Amirtharaj [a& b*] and M. Mariappan [b]

[a]Department of Chemistry, T. B. M. L. College, Porayar, Tamilnadu, India-609307

[a]Department of Chemistry, Thiru. Vi. Ka. Govt. Arts College, Thiruvarur, Tamilnadu, India-610003

Corresponding author email: snelsamir@gmail.com

Abstract

Mn_2O_3 is a significant candidate for various applications. In the present work, the Mn_2O_3 nanorod arrays have been successfully prepared through facile sonochemical method with the aid of cetyl trimethyl ammonium bromide (CTAB) template. The crystalline phase and bonding properties have ben confirmed through X-ray diffraction analysis (XRD) and Fourier transform infrared (FTIR) spectroscopic analysis. The electrochemical properties were analysed through various techniques such as cyclic voltammetric and galvanostatic charge/discharge analysis. Interestingly, cyclic voltammetric (CV) curves confirms the electric double layer capacitor-based charge storage mechanism and it render the maximum specific capacitance of 647 Fg^{-1} at a scan rate 5 mVs^{-1} whereas the galvanostatic charge/discharge studies offer the specific capacitance of 656 Fg^{-1} at a current density of 1 Ag^{-1}. The Mn_2O_3 nanorod arrays provide the maximum energy and power densities of 91.1 Wh Kg^{-1} and 14985 Wkg^{-1} respectively. In addition, the cyclic stability analysis exhibit only 12 % initial capacitance degradation over 3000 CV cycles at a scan rate of 100 mVs^{-1}. The hopeful outcomes demonstrate the significant of the Mn_2O_3 nanorod arrays as electrode material for supercapacitor devices.

Keywords: Mn_2O_3 nanorod arrays; energy storage; Supercapacitor; sonochemical

1. Introduction

Developing innovative energy storage devices has become a significant challenge due to the rising of modern technological revolution and over-consumption of natural resources especially fossil fuels[1,2]. Supercapacitors have drawn tremendous interest, because of their attractive features such as rapid charge/discharge, extended cycle life and high-power density. As a modern energy storage system, supercapacitors have played a significant role in various application areas such as hybrid electric vehicle, portable electronic gadgets and other micro energy storage systems[3,4]. Supercapacitors can store charges in two different ways such as electric double layer capacitor and pseudocapacitor mechanisms. The capacitance of electric double layer capacitors resulting from adsorption of ions at the electrode /electrolyte interface whereas redox reaction produce capacitance in pseudocapacitors which occur between electrode and electrolyte[5,6]. Carbon based substances (activated carbon, carbon aerogel, carbon nanotube and graphene oxide) are generating electric double layer capacitors while metal oxides and conducting polymers generating pseudocapacitance[7,8]. Till now, various types of materials have been extensively utilized as supercapacitor electrode materials. Particularly, different transition metal oxides such as ruthenium-based materials, NiO[9], Co_3O_4[10], MoO_3[11], MnO_2[12], V_2O_5[13], SnO_2[14], Nb_2O_5 [15] and TiO_2[16] have been generally demonstrated as supercapacitor electrode materials owing to their low cost, environmental friendliness, high redox activity and easy abundance in nature.

Manganese oxide based materials such as MnO_2, Mn_2O_3 and Mn_3O_4 are a suitable choice for successful supercapacitive electrode materials among these transition metal oxide substances owing to their various oxidation states, attractive structural features, low toxicity nature and excellent chemical and physical stability in different kinds of electrolytes[17]. Compared to the other traditional electrode substances, the Mn_2O_3 has received considerable interest in the area of energy storage devices owing to its interesting electrochemical features, superior theoretical capacitance value, high valency of manganese material, significant

structural features, easy preparation process and environmental compatibility[18,19]. On the other hand, Mn_2O_3 has not been demonstrated as a good electrode substance for supercapacitors because of their uneven morphological features, low ionic conductivity, low porosity and poor cyclic stability. In addition, the volume of Mn_2O_3 has been expanded during the cyclic stability process, which restricted the performance of the supercapacitor devices[20,21]. Different techniques have been employed to overcome these disadvantages and alter Mn_2O_3 into significant supercapacitor electrode substance. Increased the specific surface area and tuning the morphological properties is the finest remedy to increase the utilization Mn_2O_3 into supercapacitor electrode materials.

Various synthetic methodologies have been utilized to alter the morphological properties of Mn_2O_3 materials. For example, the hydrothermal method was employed to prepare Mn_2O_3 nanocubics structure followed by annealing process, which render the specific capacitance of 191.1 Fg^{-1}, high rate capability and superior cycle life[22]. Xu et al[23] demonstrated Mn_2O_3 microsheet arrays on nickel foam using mild chemical reaction united with a heat treatment progression. The microsheet arrays offer the specific capacitance of 566.6 F g^{-1}, superior energy (19.65 Wh kg^{-1}) and power (124 W kg^{-1}) densities. Kharade et al [24]established the manganese oxide nanoflake structure via galvanostatic electrodeposition synthetic approach which exhibits the specific capacitance of 414 Fg^{-1} with 86 % cyclic retention.

Among the synthetic methodologies, the sonochemical approach is a useful, cost effective, less time-consuming technique for preparing nanosized materials with different morphologies and unique characteristics. It supports the large scale synthesis of various nanomaterials. The sonochemical method is based on the physical phenomena of acoustic cavitation ensuing from continuous bubbles generation, development and implosive collapse of bubbles in a liquid medium. Extreme heating, pressure and high cooling rates are produced

during bubbles collapsing process. The transient, localized hot spots can initiative various chemical process and provide different type of nanostructures[25]. Till now, different kinds of nanostructures (nanorods [26], nanoflowers [27], nanoplates[28], nanofibers[29], nanocubes[30], nanofires[31] and nano petal[32]) have been prepared using the sonochemical synthetic approach.

In this work, the Mn_2O_3 nanorod arrays were demonstrated using sonochemical approach combined with calcination process. The cetyl trimethyl ammonium bromide (CTAB) template was used to restrict the aggregation during the synthesis process and it also tuned the morphological properties of the Mn_2O_3 materials. The x-ray diffraction analysis and Fourier transform infrared spectroscopic analysis confirms the formation of Mn_2O_3 materials. The nanorod arrays morphology was confirmed through high resolution scanning electron microscopy. The electrochemical properties of Mn_2O_3 materials were analysed via cyclic voltammetric and galvanostatic charge/discharge analysis. The CV curve provide the specific capacitance of 647 Fg^{-1} at 5 mVs^{-1} where GCD exhibit the specific capacitance of 656 Fg^{-1} at 1 Ag^{-1} with 89 % capacitance retention till 3000 cyclic voltametric cycles at a scan rate of 100 mVs^{-1}. These results confirmed that the freshly prepared Mn_2O_3 nanorod arrays is a good electrode material for supercapacitor device applications.

2. Experimental section

2.1.Materials

All reagents were analytical grade and employed without further purification. Manganese acetate tetrahydrate ($MnC_2H_6O_4{\cdot}4H_2O$), cetyl trimethyl ammonium bromide (CTAB) and ethanol were acquired from SRL (India). Carbon black, polyvinylidine difluoride (PVdF), N-methyl-2- pyrrolidone (NMP) were procured Sigma Aldrich, India. Stainless steel foil, Potassium hydroxide and sodium sulfate (Na_2SO_4) were purchased from Alfa aeser.

2.2. Synthesis of Mn_2O_3 material

In a typical synthesis, 0.01 m of cetyltrimethylammonium bromide (CTAB) was dissolved in a 100 mL of DI to form a homogeneous solution. After that, O.5 M of manganese acetate tetrahydrate precursor was dissolved in 100 ml of De-ionized water and it was added to CTAB solution. In this mixture, 10 ml of 2 M NaOH was added and stirred for 10 min. to occur precipitation process. Then, it was transferred to the ultrasonicator and sonicate for 0, 20 and 40 min for Mn_2O_3-1, Mn_2O_3-2 and Mn_2O_3-3 materials. The final products were collected by centrifugation and washed with deionized water and ethanol respectively. The resultant samples were dried in an oven at 70 °C for 12 h and it was annealed at 300 °C for 3h to get the final product.

2.3.Material characterization and electrode preparation

The BRUKER D8 Advance instrument with Cu-Kα radiation ((λ=0.154060 nm) was used to analyse the x-ray diffraction analysis whereas the FTIR analyses were done in SHIMADZU model IR Affinity 1 instrument. High resolution scanning electron microscopy (F E I Quanta FEG 200 instrument) were used to characterize the morphological features of Mn_2O_3 materials. The supercapacitive properties were analysed through cyclic voltammetric and galvanostatic charge/discharge analyses. All the electrochemical analysis were done in three electrode electrochemical cell (Biologic SP-150) with the aid of 1 M Na_2SO_4 electrolyte. The platinum wire, saturated calomel electrode and active material coated stainless steel foil were used as counter reference and working electrodes respectively. The working electrode was prepared by mixing of active material, acetylene black and poly (vinylidene fluoride) (80:10:10) in N-methyl-2-pyrrolidone (NMP) solvent. The resultant slurry was uniformly coated on the stainless steel foil and dried in a vacuum oven at 70 °C for 12 h to get the working electrodes. The weight of the active material was approximately 4 mg.

3. Results and discussion

3.1. X-ray diffraction analysis

X-ray diffraction patterns of the freshly prepared Mn_2O_3-1, Mn_2O_3-2 and Mn_2O_3-3 materials were recorded to identify crystal phase features as presented in fig. 1 a-c. The diffraction patterns of the Mn_2O_3 matches with the cubic crystal structure of Mn_2O_3 (JCPDS card No.-041-1442) and shown various peaks at 2θ value of 23.1°, 32.9°, 38.2°, 42.9°, 45.1°, 49.3°, 53.2°, 55.1°, 60.6°, 64°, 65.8°, 67.4°, 69.1° and 73.9° are resembles to (211), (222), (400), (420), (332), (431), (521), (440), (611), (541), (622), (631), (444) and (721) plans respectively. All the x-ray diffraction patterns provide similar spectrum whereas the intensity only varies. The absence of impurity peaks indicates that the present CTAB assisted sonochemical synthetic approach generates highly pure Mn_2O_3 materials. The result confirms the formation of highly pure Mn_2O_3 materials and it related to the previous literature also[33].

3.2. FTIR analysis

FTIR spectra of the Mn_2O_3-1, Mn_2O_3-2 and Mn_2O_3-3 materials are shown in the fig. 2 a-c respectively. The FTIR spectrum are recorded to verify the bonding characteristics of the Mn_2O_3 materials. All the FTIR spectrum exhibits six peaks located at 3426, 1643, 1394, 1029, 634, 520 cm^{-1} are corresponding to various bonding nature of surface absorbed water molecule and Mn_2O_3 respectively. The peak located at 3426 is ascribed to stretching vibration of -OH group. The peak visible at 1643 cm^{-1} attributes the adsorption of moisture on the surface of the materials whereas the peaks present at 1394 and 1029 cm^{-1} indicates the combined bending vibrations of the Mn atoms with -OH groups. The bands appeared at 634 and 520 cm^{-1} attributes the stretching modes of tetrahedral and octahedral sites in Mn-O bonds respectively[34,35].

3.3.Morphological analysis

The morphological features of the Mn_2O_3 materials plays a significant role in the electrochemical characteristics and it analysed using HR- SEM analysis (fig 3 a-f). Figure 3 a and b shows the lower and higher magnification HR-SEM images of the Mn_2O_3-1 material which shows definite shaped nanoparticle structure with the size of 120 ±10 nm. The small

amount of nanorods also formed in between the nanoparticles. Interestingly, small such nanoparticles with a size of 12 ±5 nm were grown on the outer region of both nanoparticles and nanorods which may lead to rising the specific surface area for electrochemical process. The number of nanorods are increased when introducing 20 min of sonication (Mn_2O_3-2) which is perfectly visible in fig. 3 c and d. Fascinatingly, the amount and size of the nanoparticles are also getting decreased. Figure 3 e and f shows the HR-SEM images of the Mn_2O_3-3material which synthesized using 40 min. of sonication process. The nanorod arrays are uniformly form with the size and length of 170 ±10 nm and 700 ±10 nm respectively. The small number of nanoparticles are perfectly visible instead of nanorods also. These outcomes confirm that the present CTAB assisted sonochemical synthetic route having more impact on the morphological feature of Mn_2O_3 materials.

3.4.Electrochemical analysis

The electrochemical properties of freshly prepared Mn_2O_3 materials were analysed using cyclic voltametric and galvanostatic charge/discharge analysis. Cyclic voltammetric techniques is a powerful tool to analyse redox properties, charge storage mechanism, specific capacitance and rate capability of the electrode materials. Figure 4 a-c shows the cyclic voltammetric curves of the Mn_2O_3-1, Mn_2O_3-2 and Mn_2O_3-3 materials respectively. CV analyses were recorded within in a potential limit from 0 to 1 V at six different sweep rates such as 5, 10, 25, 50, 70, 100 mVs^{-1}. Additionally, 1 M Na_2SO_4 was used as an electrolyte for entire electrochemical analysis. All the CV curves exhibit rectangular shape, which confirms the electrochemical double layer capacitor behaviour with rapid charge transport properties[36]. The electrochemical performance of the CV curves increased with rising of scan rate from 5 to 100 mVs^{-1} which is due to the rapid ionic and electronic transport across the surface of the electrode. The shape profile of the CV curves are remain same at higher scan rates confirming the high stability and fast charge transport feature of the electrodes

materials[22]. Generally, the area under the CV curve of electrode material is directly proportional to the specific capacitance feature. In the present endeavour, the Mn_2O_3-3 electrode material possesses high area under the CV curve when compared to Mn_2O_3-1 and Mn_2O_3-2 electrodes, confirming superior specific capacitive feature of the Mn_2O_3-3 electrodes. The specific capacitance of the CV curve is calculated using the equ. 1. [37]

$$Cs = \frac{\int idv}{2*S*M*V} \quad (1)$$

Where *Cs* is the specific capacitance (Fg^{-1}), *∫idV* is the integrated area of CV curves in the cyclic voltammogram, S is the scan rate ($mV\ s^{-1}$), M is the active mass of the electrode material (g), and V is the applied potential window (V). The specific capacitance values of Mn_2O_3-1, Mn_2O_3-2 and Mn_2O_3-3 electrodes are were calculated to be 272, 524 and 647 Fg^{-1} respectively at a scan rate of 5 mVs^{-1}. The rate capability of all Mn_2O_3 electrode materials were studied using sweep rate vs specific capacitance graph as shown in fig. 4 d. Due to time limitation progression, the scan rate decreases with rising of scan rate from 5 to 100 mVs^{-1}[38].

The galvanostatic charge/discharge studies of all Mn_2O_3 electrodes were demonstrated at various current densities such as 1, 2, 3, 10 and 30 Ag^{-1} and it shown in fig. 5 a-c. It is perfectly visible that all the charge discharge curves are exhibiting triangular shape, which confirms the electric double layer-based charge storage mechanism and it is more reliable with CV results. The charge curves can be seen to be symmetrical to their respective discharge equivalents, further suggesting their outstanding reversibility and ideal electrochemical capacitive features of the Mn_2O_3 electrodes[39]. The charge/discharge curve of Mn_2O_3 -3 electrode possesses the larger time then remaining electrodes such as (Mn_2O_3 -1 and Mn_2O_3 -2) confirms the high specific capacitance behaviour of the Mn_2O_3 -3 electrode. The specific capacitance has been estimated from the galvanostatic charge/discharge studies by the equ.2.

$$Cs = \frac{I\Delta t}{m\Delta V} \quad (2)$$

Where *Cs* is the specific capacitance (Fg^{-1}), *I* is the current density (Ag^{-1}), Δt is the discharge time (s), *m* is the mass of the active materials and ΔV is the potential window. The Mn_2O_3-1, Mn_2O_3-2 and Mn_2O_3-3 electrodes render the maximum specific capacitance of 262, 550 and 656 Fg^{-1} respectively at a current density of 1 Ag^{-1}. The high specific capacitance of Mn_2O_3-3 (656 Fg^{-1}) is higher when compared to literatures based on Mn-based metal oxides (Mn_3O_4 thin films (194 Fg^{-1})[40], Mn_3O_4 nanowires on reduced graphene oxide (437 Fg^{-1}) [34], Mn_3O_4 nanoparticles (144.5 Fg^{-1})[35], Mn_3O_4 (109 Fg^{-1}) [41], Mn_2O_3 microsheet arrays (566.6 Fg^{-1}) [23], Mn_2O_3 nanocubics (191 Fg^{-1})[22], Mn_2O_3 nanoparticles (460 Fg^{-1})[19] and Mn_2O_3 nanoflakes (414 Fg^{-1})[24]). The superior specific capacitance features might accredit to the following motives: (i) Generally, one-dimensional nanorods possessing more surface area than any other nanoscale dimensions, which render the high electroactive sites and thus enhancing specific capacitance. (ii) The nanorods connected to neighbourhood nanorods and forms nanorod arrays, which is expected to favour the transport of electrolyte ions, providing admittance to more reaction spots and thus enhancing the supercapacitive features. (iii) The lower dimension of the nanorod arrays would proficiently shorten the path length for improving ion movement during electrochemical process. (iv) The small nanoparticles are present between the nanorod arrays are reducing the distance between two nanorod arrays and thus would help to the transportation of electrolyte ions without any contravention. This continuous transportation of electrolyte ion process could enhance the supercapacitive properties of the electrode materials.

The specific capacitance vs current density graph is shown in fig. 5 d. The resultant specific capacitance values were found to be decrease when rising of current density from 1 to 30 Ag^{-1} and this outcome is well agreed with the CV results. At lower current densities, the larger time would allow the effective participation of all electrode materials in electrochemical

process but it is not probable for high current densities. Consequently, the specific capacitance is lower at high current densities[42].

In supercapacitors, the energy and power density factors are very significant. The energy and power densities can be obtained by charge discharge curves and it calculated using the following equations 3 and 4. (shown in fig. 6)

$$E = \frac{1}{2}\frac{C \times V^2}{3.6} \quad (3)$$

$$P = \frac{E \times 3600}{t} \quad (4)$$

Where E is energy density (Wh Kg^{-1}), C is the specific capacitance (F g^{-1}), V Potential window (V), P power density (W Kg^{-1}), and t is the discharge time (in seconds). The Mn_2O_3-1, Mn_2O_3-2 and Mn_2O_3-3 electrodes provide the energy densities of 36.3, 76.3 and 91.1 Wh Kg^{-1} respectively at a current density of 1 Ag^{-1}. On the other hand, 14876, 14976 and 14985 Wkg^{-1} of power densities were obtained from Mn_2O_3-1, Mn_2O_3-2 and Mn_2O_3-3 electrodes respectively. Due to superior morphological features, the energy and power density factors are higher for Mn_2O_3-3 electrode when compared to Mn_2O_3-1 and Mn_2O_3-2 electrode materials.

The cyclic stability testing was carried out for all Mn_2O_3 electrodes using cyclic voltammetric analysis at a scan rate of 100 mVs^{-1} for 3000 continuous cycles as shown in fig. 7 a. Figure 7 b, c and d are corresponds to 1st and 3000th cycles of cyclic stability studies. The specific capacitances are gradually decreased and withstand 82% (Mn_2O_3-1), 86% (Mn_2O_3-2) and 88 % (Mn_2O_3-3) of initial capacitance till 3000 continuous cycles. This result establishing the good cyclic stability behaviour of the Mn_2O_3-3 electrode materials and signifying the potential to be utilized for supercapacitor electrode materials.

4. Conclusion

In summary, the Mn_2O_3 nanorod arrays were successfully synthesised using sonochemical method with the aid CTAB template. The Mn_2O_3 materials were calcined at 300

°C to get the final product. The crystalline behaviour and bonding nature of the prepared materials were characterized using XRD and FTIR techniques, which are confirmed the formation of Mn_2O_3 materials. The HR-SEM was used to characterize the surface morphological features and it confirms the nanorod arrays structure. The CV and GCD analysis were carried out to examine the electrochemical properties. The CV curves provide the maximum specific capacitance of 647 Fg^{-1} at a scan rate of 5 mVs^{-1} while the GCD curves exhibit 656 Fg^{-1} at a current density of 1 Ag^{-1} respectively. In addition, the energy and power density feature of were also calculated and it attained the 91.1 Wh Kg^{-1} and 14985 Wkg^{-1} respectively. The cyclic stability studies show only 12 % reduction and withstand 88% of initial capacitance till 3000 CV cycles at scan rate of 100 mVs^{-1}. Such significant outcomes of electric double layer capacitive Mn_2O_3 nanorod arrays is the potential electrode materials for supercapacitor application.

Conflicts of interest

There are no conflicts to declare.

References

1. M. R. Benzigar, V. D. B. C. Dasireddy, X. Guan, T. Wu, and G. Liu, Adv. Funct. Mater. **30**, (2020).

2. C. Kang, J. Fang, L. Fu, S. Li, and Q. Liu, Chem. - A Eur. J. **26**, 16392 (2020).

3. C. Ren, X. Jia, W. Zhang, D. Hou, Z. Xia, D. Huang, J. Hu, S. Chen, and S. Gao, Adv. Funct. Mater. **30**, 1 (2020).

4. Q. Zhu, D. Zhao, M. Cheng, J. Zhou, K. A. Owusu, L. Mai, and Y. Yu, Adv. Energy Mater. **9**, 1 (2019).

5. S. K. Balasingam, S. Lee, and Y. Jun, 15491 (2015).

6. S. S. Patil, D. P. Dubal, V. G. Deonikar, M. S. Tamboli, J. D. Ambekar, P. Gomez-Romero, S. S. Kolekar, B. B. Kale, and D. R. Patil, ACS Appl. Mater. Interfaces **8**, 31602 (2016).

7. Q. Zhang, J. Zhao, Y. Wu, J. Li, H. Jin, S. Zhao, L. Chai, Y. Wang, Y. Lei, and S. Wang, Small **16**, 1 (2020).

8. C. Zhang, Q. Chen, and H. Zhan, ACS Appl. Mater. Interfaces **8**, 22977 (2016).

9. J. W. Lang, L. Bin Kong, W. J. Wu, Y. C. Luo, and L. Kang, Chem. Commun. 4213 (2008).

10. S. Xiong, C. Yuan, X. Zhang, B. Xi, and Y. Qian, Chem. - A Eur. J. **15**, 5320 (2009).

11. S. Liu, C. Xu, H. Yang, G. Qian, S. Hua, J. Liu, X. Zheng, and X. Lu, Small **16**, 1 (2020).

12. P. Yu, X. Zhang, Y. Chen, and Y. Ma, Mater. Lett. **64**, 61 (2010).

13. J. Yang, T. Lan, J. Liu, Y. Song, and M. Wei, Electrochim. Acta **105**, 489 (2013).

14. Y. Kang, Z. Li, K. Xu, X. He, S. Wei, and Y. Cao, J. Alloys Compd. **779**, 728 (2019).

15. F. Idrees, J. Hou, C. Cao, F. K. Butt, I. Shakir, M. Tahir, and F. Idrees, Electrochim. Acta **216**, 332 (2016).

16. H. Zhou and Y. Zhang, J. Phys. Chem. C **118**, 5626 (2014).

17. M. S. Kolathodi, S. N. Hanumantha Rao, T. S. Natarajan, and G. Singh, J. Mater. Chem. A **4**, 7883 (2016).

18. S. Z. Huang, J. Jin, Y. Cai, Y. Li, Z. Deng, J. Y. Zeng, J. Liu, C. Wang, T. Hasan, and B. L. Su, Sci. Rep. **5**, 1 (2015).

19. Y. H. Son, P. T. M. Bui, H. R. Lee, M. S. Akhtar, D. K. Shah, and O. B. Yang, Coatings **9**, (2019).

20. J. Liang, L. T. Bu, W. G. Cao, T. Chen, and Y. C. Cao, J. Taiwan Inst. Chem. Eng. **65**, 584 (2016).

21. S. Maiti, A. Pramanik, and S. Mahanty, CrystEngComm **18**, 450 (2016).

22. W. Li, J. Shao, Q. Liu, X. Liu, X. Zhou, and J. Hu, Electrochim. Acta **157**, 108 (2015).

23. J. Xu, Y. Sun, M. Lu, L. Wang, J. Zhang, J. Qian, and E. J. Kim, J. Alloys Compd. **717**, 108 (2017).

24. P. M. Kharade, S. B. Kulkarni, and D. J. Salunkhe, Chinese J. Phys. **55**, 1684 (2017).

25. K. S. Suslick, (1990).

26. J. Yesuraj, A. S. Samuel, E. Elaiyappillai, P. M. Johnson, V. Elumalai, and M. Bhagavathiachari, J. Electroanal. Chem. **797**, 78 (2017).

27. A. A. Yadav, Y. M. Hunge, and S.-W. Kang, Ultrason. Sonochem. **72**, 105454 (2021).

28. S. Palanisamy, S. Velmurugan, and T. C. K. Yang, Ultrason. Sonochem. **64**, 105043 (2020).

29. R. R. Huerta, E. K. Silva, I. Ekaette, T. El-Bialy, and M. D. A. Saldaña, Ultrason. Sonochem. **64**, 104759 (2020).

30. K. Kaviyarasan, S. Anandan, R. V. Mangalaraja, T. Sivasankar, and M. Ashokkumar, Ultrason. Sonochem. **29**, 388 (2016).

31. M. Park, Y. Sohn, W. G. Shin, J. Lee, and S. H. Ko, Ultrason. Sonochem. **22**, 35 (2015).

32. L. Jafari Foruzin and Z. Rezvani, Ultrason. Sonochem. **64**, 104919 (2020).

33. N. F. M. Yusoff, N. H. Idris, M. F. M. Din, S. R. Majid, N. A. Harun, and M. M. Rahman, Sci. Rep. **10**, 1 (2020).

34. G. Bharath, N. Arora, A. Hai, F. Banat, D. Savariraj, H. Taher, and R. V. Mangalaraja, Electrochim. Acta **337**, 135668 (2020).

35. E. R. Kavitha, S. Meiyazhagan, S. Yugeswaran, P. Balraju, and K. Suresh, Int. J. Energy Res. 1 (2020).

36. H. Jiang, C. Zhou, X. Yan, J. Miao, M. You, Y. Zhu, Y. Li, W. Zhou, and X. Cheng, J. Energy Storage **32**, 101898 (2020).

37. M. Marimuthu, S. Ganesan, and J. Y. Johnbosco, Electrochim. Acta **357**, 136848 (2020).

38. S. K. Balasingam, M. Lee, B. H. Kim, J. S. Lee, and Y. Jun, Dalt. Trans. **46**, 2122 (2017).

39. R. Wang, M. Han, Q. Zhao, Z. Ren, X. Guo, C. Xu, N. Hu, and L. Lu, Sci. Rep. **7**, 1 (2017).

40. A. C. Nkele, U. Chime, B. Ezealigo, A. Nwanya, A. C. Agbogu, A. B. C. Ekwealor, R. U. Osuji, P. M. Ejikeme, M. Maaza, and F. Ezema, J. Mater. Res. Technol. **9**, 9049 (2020).

41. N. Maile, S. K. Shinde, S. S. Patil, D. Y. Kim, A. V. Fulari, D. S. Lee, and V. J. Fulari, Ceram. Int. **46**, 14640 (2020).

42. J. Yesuraj, S. Austin Suthanthiraraj, and O. Padmaraj, Mater. Sci. Semicond. Process. **90**, 225 (2019).

Figures

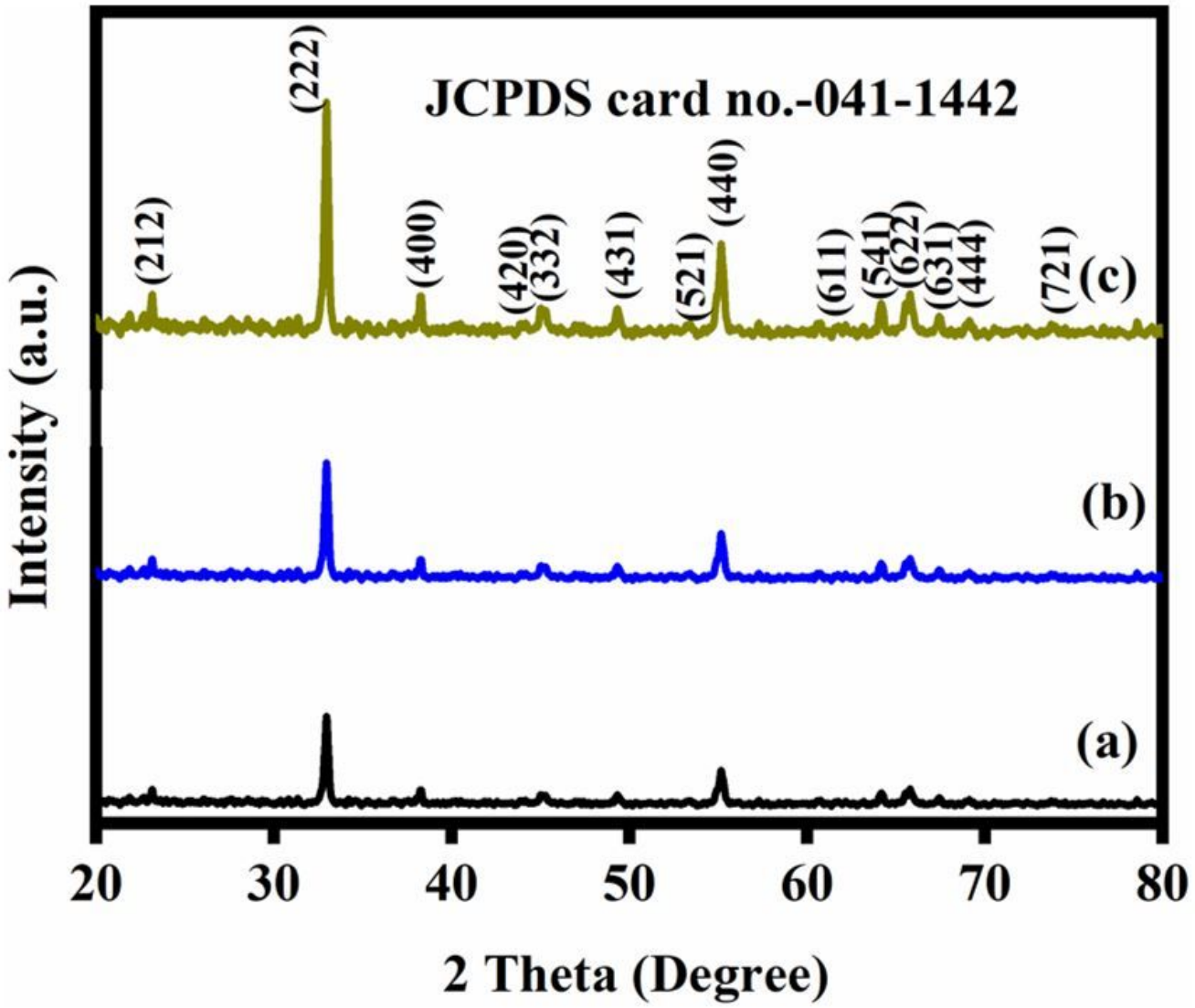

Figure 1

XRD analysis of Mn2O3 materials. (a) Mn2O3-1; (b) Mn2O3-2 and (c) Mn2O3-3

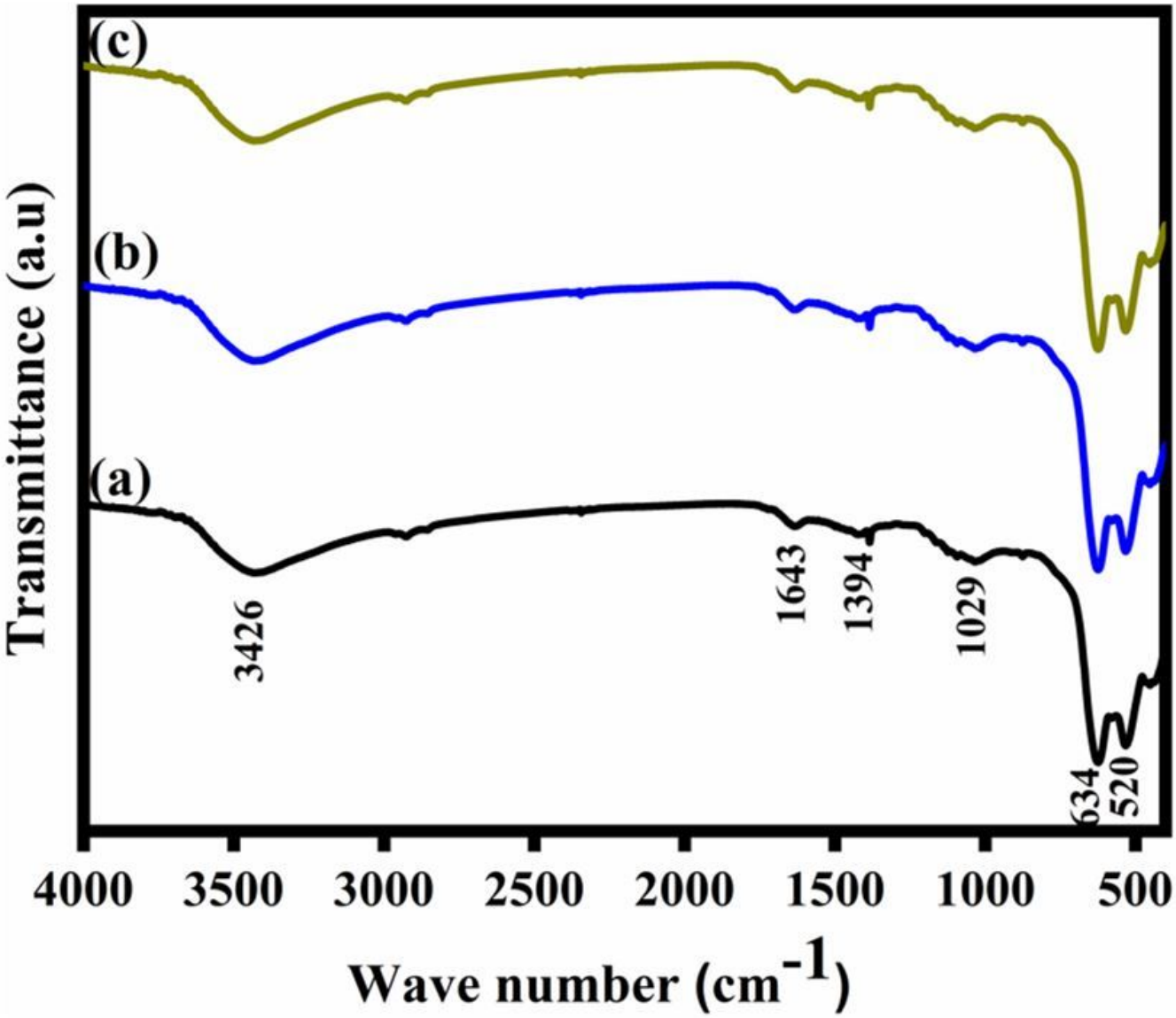

Figure 2

FTIR analysis of Mn2O3 materials. (a) Mn2O3-1; (b) Mn2O3-2 and (c) Mn2O3-3

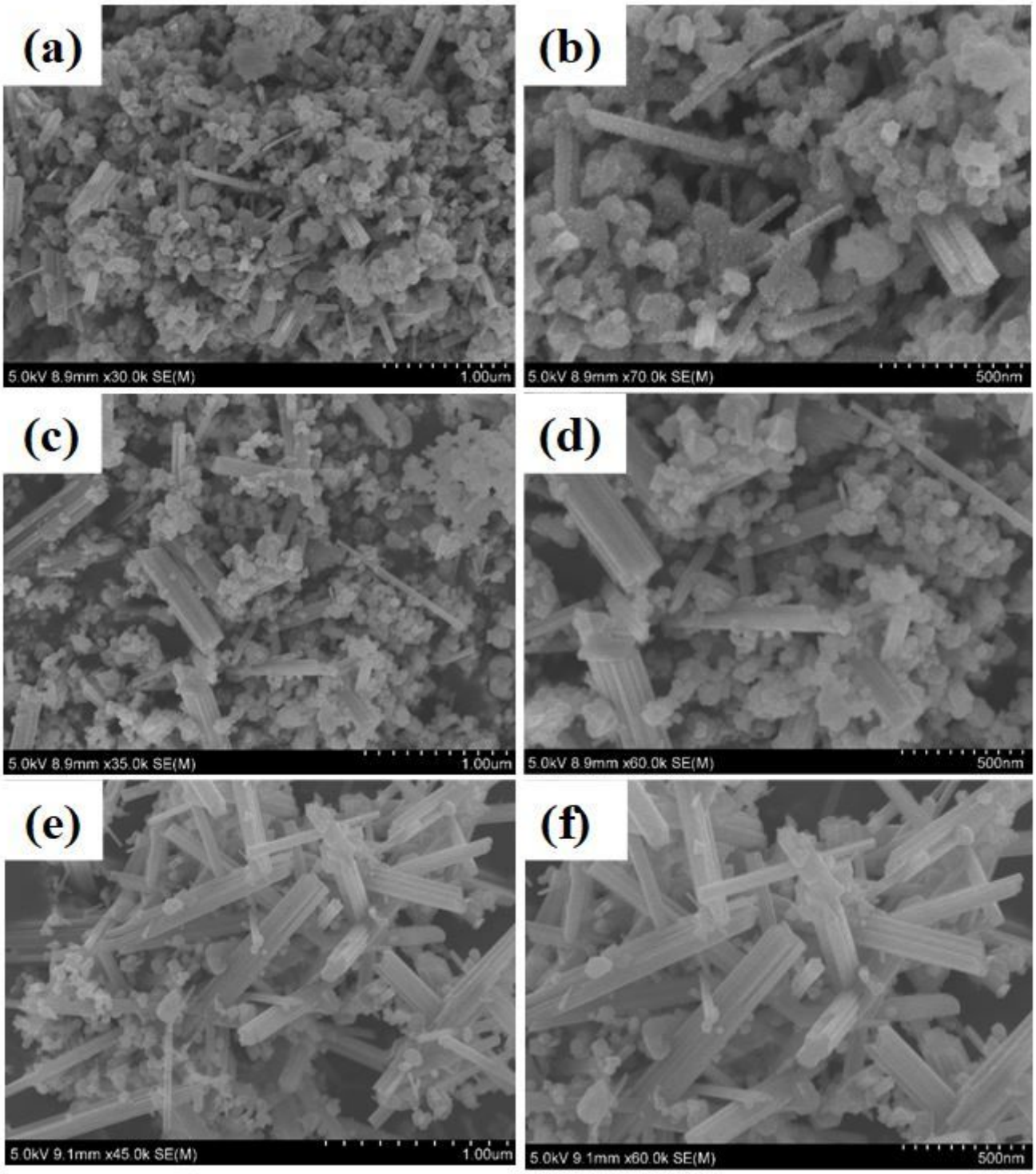

Figure 3

Lower and higher magnification HR-SEM images of Mn2O3 materials. (a) & (b) Mn2O3-1; (c) & (d) Mn2O3-2 and (e) & (f) Mn2O3-3

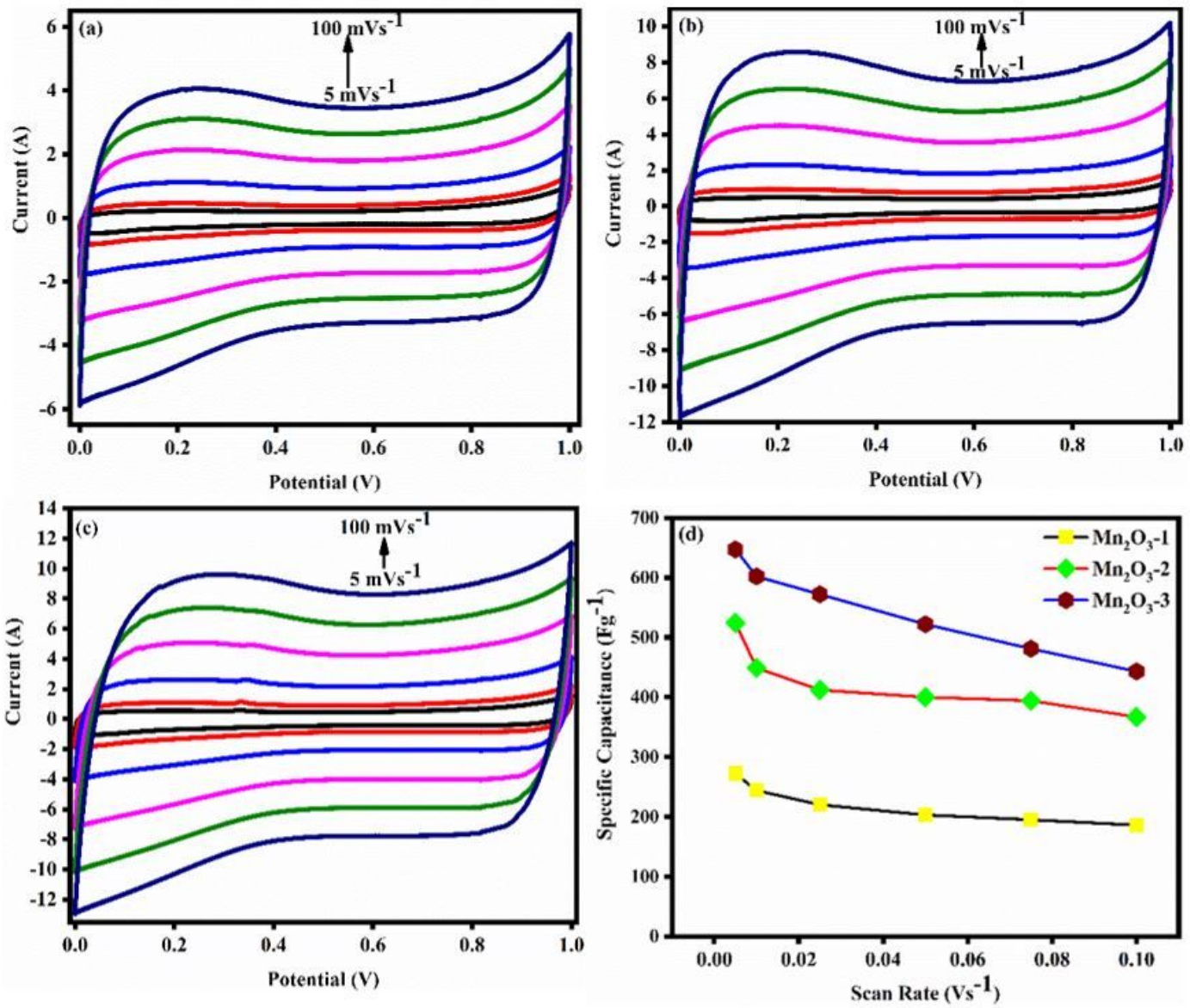

Figure 4

CV curves of (a) Mn2O3-1; (b) Mn2O3-2 and (c) Mn2O3-3 materials and (d) specific capacitance vs scan rate

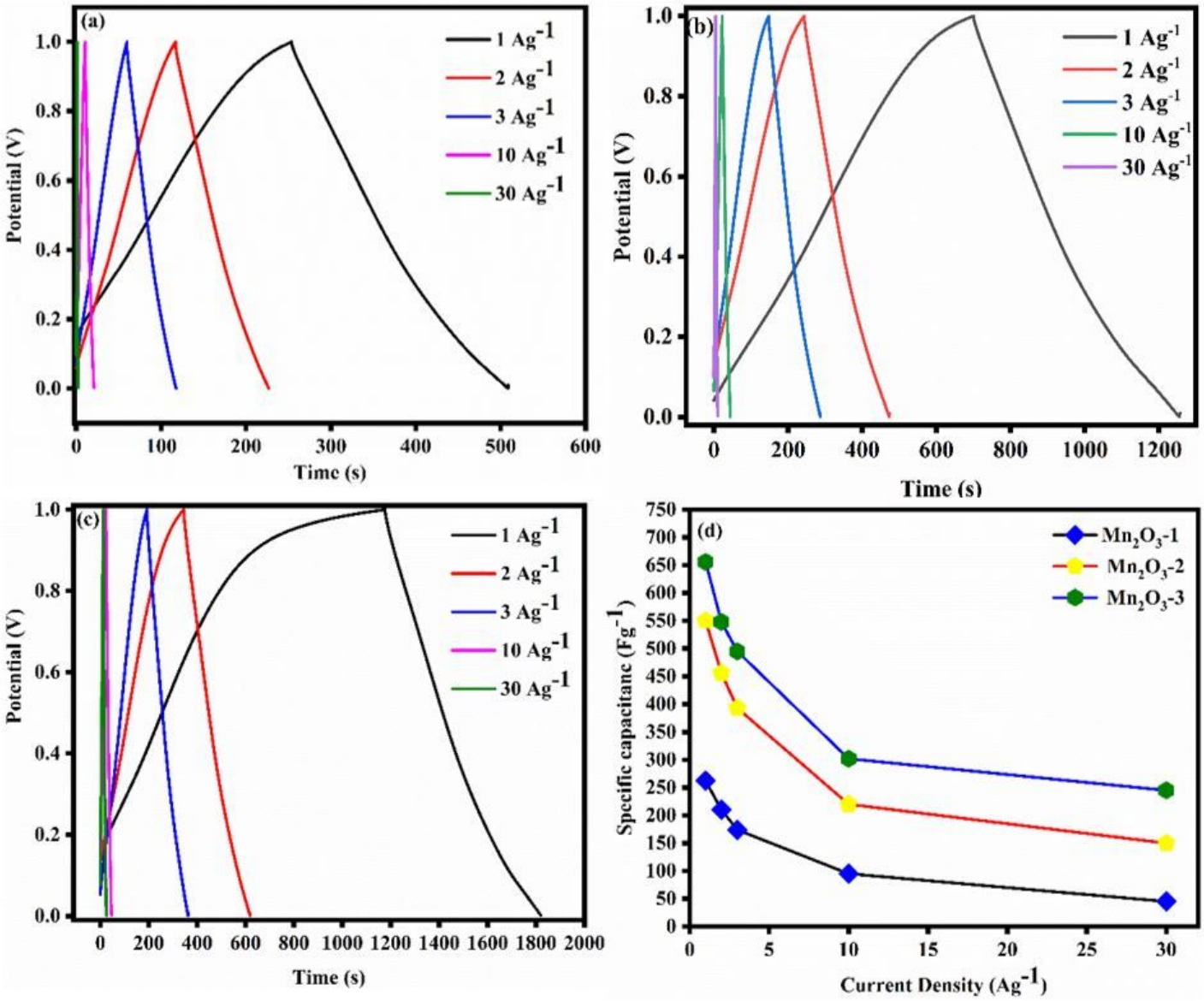

Figure 5

GCD curves of (a) Mn2O3-1; (b) Mn2O3-2 and (c) Mn2O3-3 materials and (d) specific capacitance vs current density

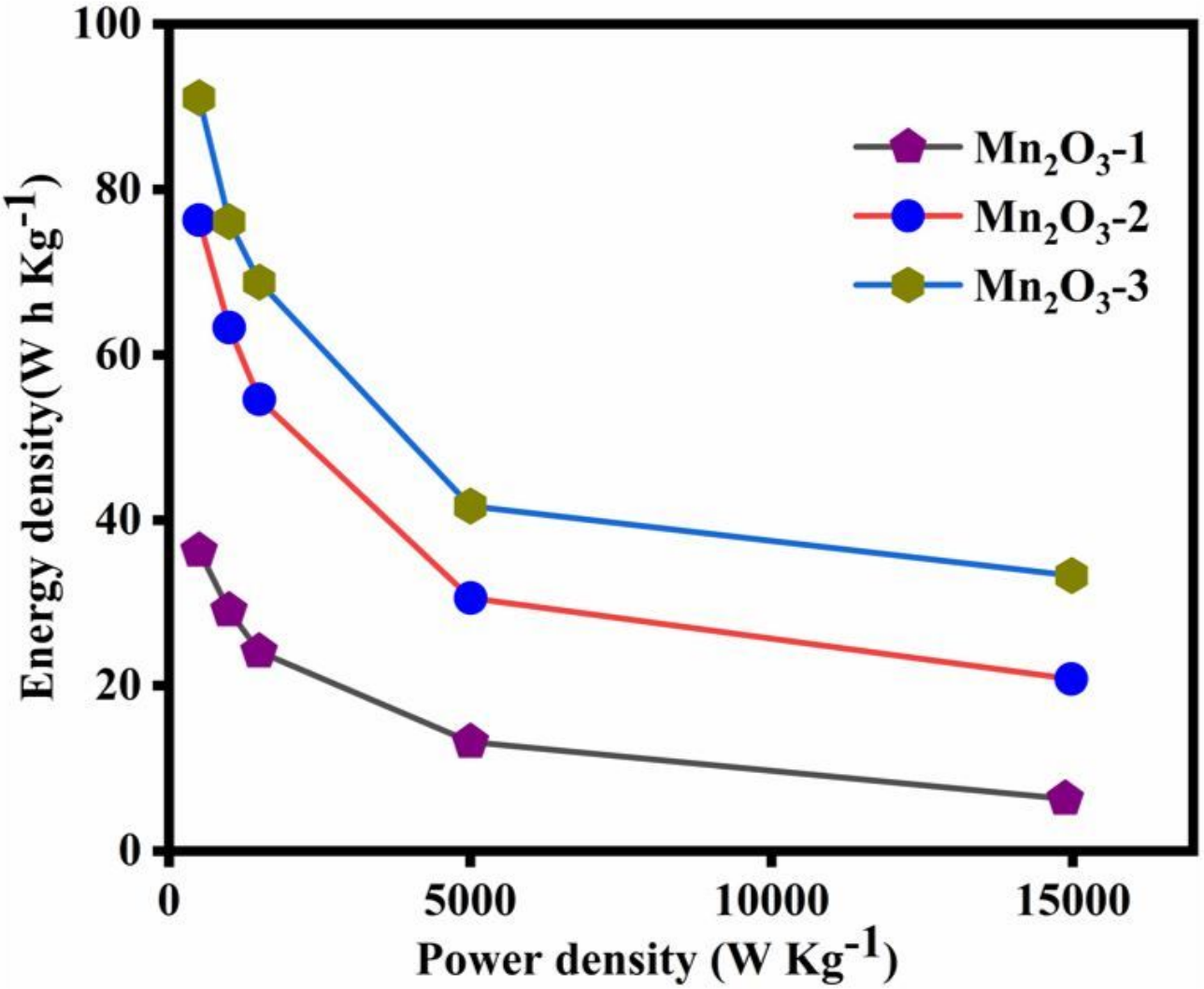

Figure 6

Ragone plot Mn2O3 materials

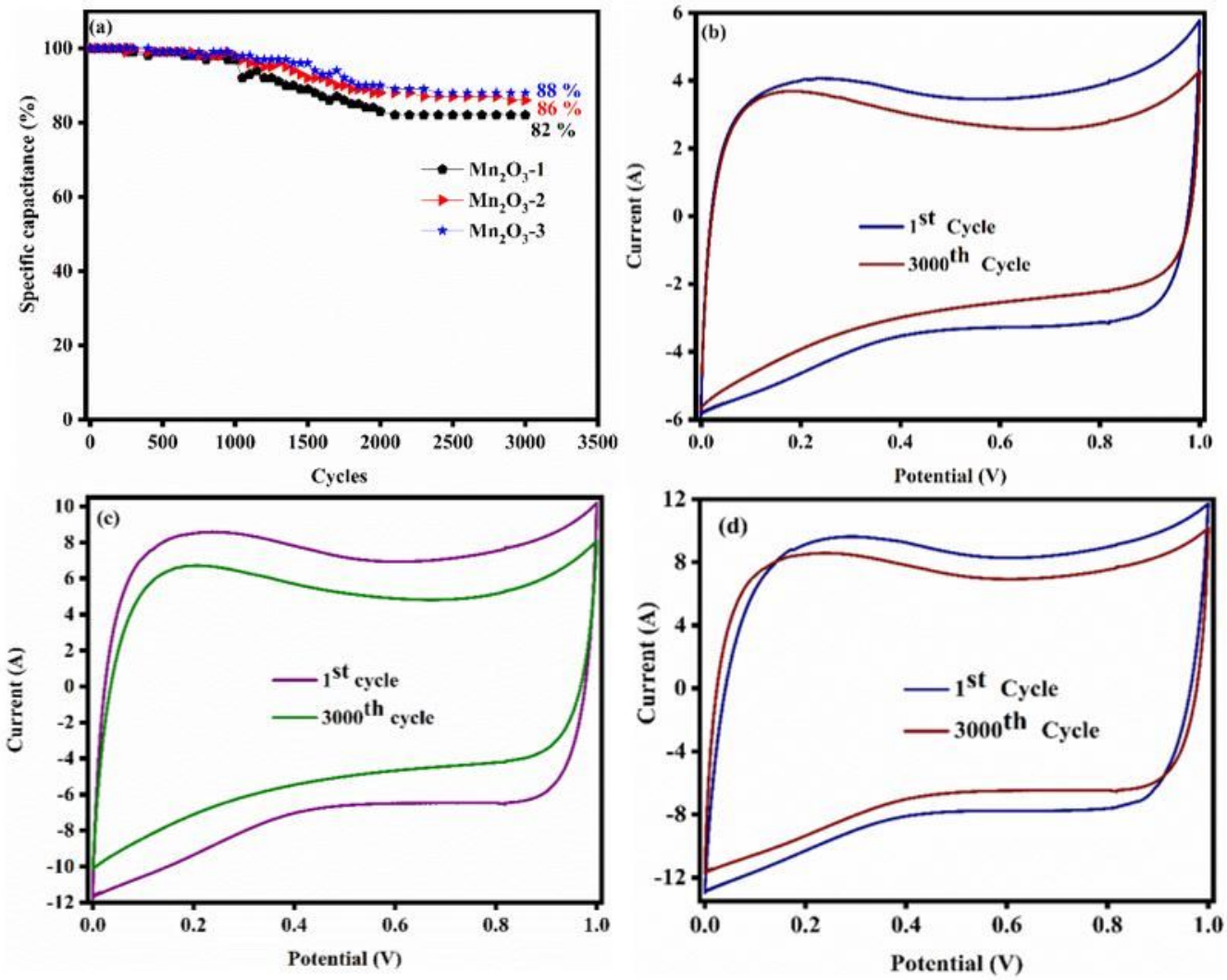

Figure 7

(a) Cycle life test of Mn2O3 materials at a san rate of 100mVs-1. 1st and 3000th CV curves of (a) Mn2O3-1; (b) Mn2O3-2 and (c) Mn2O3-3 materials